Model Predictive Current Control With Model-Aid Extended State Observer Compensation for PMSM Drive

Huanli Liu, Weiyang Lin, *Member, IEEE*, Zhitai Liu, *Student Member, IEEE*, Concettina Buccella, *Senior Member, IEEE*, and Carlo Cecati, *Fellow, IEEE*

***Abstract*—Model predictive current controller is a popular and effective technique to provide fast dynamic response in the field of motor control. However, conventional predictive controllers are susceptible to deteriorating control performance when model mismatch exists, such as changes in motor parameters due to the temperature variations. Therefore, this article proposes a precise model-aid extended state observer (MAESO) compensation-based real-time model predictive current controller with enhanced parameter robustness performance and high bandwidth. The predictive controller is converted into the form of multiparameter quadratic programming for online solution using numerical computational method and the constraints are linearized. In addition, the disturbances estimated by MAESO are fed back to the controller in the form of parameters for cycle-by-cycle compensation without extra controller design. Comparative simulations and experiments under different operating conditions are carried out to verify the effectiveness and superiority of the proposed method.**

***Index Terms*—Extended state observer (ESO), model predictive control, permanent magnet synchronous motor (PMSM) drive, quadratic programming.**

I. Introduction

FOR many years, permanent magnet synchronous motors (PMSM) have received continuous attention [1], [2], [3], [4] due to their high torque density, efficiency, and simple structure. They are widely used in almost all industrial fields, such as manipulator joints [5], robotics or servo systems [6], moreover they are common choice in electric vehicles [7], [8].

Manuscript received 27 July 2022; revised 16 October 2022; accepted 25 November 2022. Date of publication 30 November 2022; date of current version 26 December 2022. This work was supported in part by the Joint Funds of the National Natural Science Foundation of China under Grant U20A20188, in part by the Major Scientific and Technological Special Project of Heilongjiang Province under Grant 2021ZX05A01, and in part by the Major Scientific and Technological Research Project of Ningbo under Grant 2021Z040. Recommended for publication by Associate Editor S. A. Khajehoddin. *(Corresponding author: Weiyang Lin.)*

Huanli Liu, Weiyang Lin, and Zhitai Liu are with the Research Institute of Intelligent Control and Systems, Harbin Institute of Technology, Harbin 150001, China (e-mail: hlliu@stu.hit.edu.cn; wylin@hit.edu.cn; ztliu@hit.edu.cn).

Concettina Buccella and Carlo Cecati are with the Department of Information Engineering Computer Science and Mathematics, University of L'Aquila, 67100 L'Aquila, Italy, and also with DigiPower srl, 67100 L'Aquila, Italy (e-mail: concettina.buccella@univaq.it; c.cecati@ieee.org).

Color versions of one or more figures in this article are available at https://doi.org/10.1109/TPEL.2022.3225626.

Digital Object Identifier 10.1109/TPEL.2022.3225626

The conventional control framework of PMSM is field-oriented-control (FOC). By transforming the three-phase currents to the direct and quadrature axes currents, two proportional–integral (PI) controllers are used to control the motor [9]. However, the PI controller is essentially a model-free control method and it is difficult to enhance its performance further without any model information. Among numerous alternatives, model predictive current control (MPCC) is a suitable and attractive method to replace the conventional PI control offering enhanced robustness and bandwidth [10], [11], [12], [13]. High current loop bandwidth improves overall performance, including speed loop settling time, which is helpful for those applications that require fast response. Examples of systems requiring high bandwidth because they need the motor to reach the specified position in the fastest time, are, for instance: rapid sorting by manipulators, high-speed soldering of wire bonding machines [14], high-speed placement for chip mounters [15], and many others. Besides, high current loop bandwidth allows the outer loop gain to be reduced, while still maintaining the same performance without causing noise amplification. Therefore, it is valuable to further increase the current loop bandwidth.

According to the existing literature, MPCC can be classified into two distinct classes: finite control set MPCC (FCS-MPCC) and continuous control set MPCC (CCS-MPCC) [16], [17], [18], [19]. FCS-MPCC directly searches a finite control set of the voltage vector (VV) to find the optimal one with the help of a cost function. Since FCS-MPCC does not need the implementation of an explicit space vector pulsewidth modulation algorithm (SVPWM), its implementation is simple and straightforward. However, it suffers from large torque ripples and high losses in switching devices. Some methods have been proposed to overcome these drawbacks. In [20], zero VV was introduced and combined with the optimal VV to reduce torque ripple. Aguirre et at. [21] studied the period control approach thus ensuring invariance of the switching frequency. CCS-MPCC, instead, usually needs the solution of a convex optimization problem with constraints in a forward direction to obtain the optimal VV. The result of its calculation can be any point in the feasible region, which will significantly reduce torque ripples. After that, VV is sent to the SVPWM module after coordinate transformation. As a consequence, massive computing resources are needed for this method. Wang et al. [16] implemented an unconstrained MPCC

method using saturation modules for the controller output. The analytical solution of the optimal VV is obtained by taking the first order derivative of the cost function, thus avoiding the direct calculation of the constrained MPCC and effectively overcoming the problem of computational effort. In the case of sufficient memory, an explicit model predictive control method was proposed in [19]. After presolving the optimization problem offline, the complex calculation is simplified to a search problem and the computational burden of MPCC is greatly reduced for online solving.

Despite the remarkable performance, MPCC still relies on the accuracy of the predictive model and becomes unstable when the model parameters vary significantly. In [22] and [23], the authors used an integral action to compensate for model uncertainty and noise, which is an effective way to deal with the issue. A discrete-time disturbance observer based on the pole placement techniques [24] using nominal inductance is designed to estimate the disturbance caused by the parameter mismatch. From the perspective of the model parameters themselves [25], the online inductance extraction algorithm with sliding mode observer has been studied to gain the accurate inductance, which will be used to compensate the model error in real-time. Ma et al. [26] proposed a method of using the current gradient updating mechanism as a predictive model to achieve model-free control, thereby getting rid of the dependence on model parameters. Similarly, a recursive least-square algorithm is proposed for the prediction model [27], which also does not depend on the motor parameters. However, these methods still suffer from prediction bias in forecasting. Therefore, Zhang et al. [28] designed an extended state observer (ESO) to obtain disturbance and compensate for prediction differences due to the model-free control. Another way to eliminate the influence of parameters is to use the incremental system method [29] to eliminate the rotor flux linkage from the prediction equation, thus achieving robust performance against to the flux linkage. For the variation of other parameters, the observer is designed to compensate, which will complicate the controller design. In fact, these methods are remarkable for robustness improvement of predictive control. However, the bandwidth performance of these methods cannot be further improved due to the lack of model information.

In recent years, as the core part of the active-disturbance-rejection controller (ADRC), the ESO has been widely applied in the fields of current harmonic suppression [30], disturbance observation [31], etc. For example, in [32], the ESO is designed to estimate the external disturbance of the speed prediction model, which improved the antidisturbance performance of the speed loop significantly. However, it is difficult to increase the bandwidth of conventional ESO without model assistance for the same control period.

To increase the bandwidth of current controller and enhance the robustness of MPCC to model parameters and other nonlinearities, a real-time MPCC method with model-aid extended state observer (MAESO) compensation for PMSM drive is proposed. The main contributions of this article are as follows.

1) A precise MAESO that utilizes model information is designed to observe model mismatch as well as other disturbances, providing the controller with fast and accurate feedback values of the real system. Besides, the gain design method of the observer is also described.
2) The MPCC controller embedded with MAESO is established and uncertainty disturbances are compensated in each period to enhance the robustness of controller with model uncertainty and increase the bandwidth performance.
3) The enhanced predictive controller is adapted to the form of multi-parameter quadratic programming (MPQP) and the nonlinear constraints are approximated as polygon constraints, which effectively reduce the online computational burden of the processor.
4) The feedback values of each cycle are compensated by a one-step prediction, which improves the timeliness of the feedback values. As a result, the system bandwidth is further increased.

The rest of this article is organized as follows. In Section II, the PMSM discretization dynamic model including disturbance compensation is constructed. In Section III, the cost function for current tracking is studied to obtain an optimal incremental control sequence; the circular constraint is approximated as a polygonal linear constraint. Further, the proposed MPCC with MAESO compensation (MAESO-MPCC) method is presented in Section IV to overcome the inaccuracy of predictive model. The CCS-MPCC is modified into the form of MPQP. Finally, the simulation and experimental results performed with low power test rig are shown in Section V.

II. PMSM Dynamic Model

The PMSM model is described in dq frame as follows:

$$\begin{cases} \frac{\mathrm{d}i_\mathrm{d}}{\mathrm{d}t} = -\frac{R_\mathrm{s}}{L_\mathrm{d}} i_\mathrm{d} + \frac{L_\mathrm{q}}{L_\mathrm{d}} \omega_\mathrm{e} i_\mathrm{q} + \frac{1}{L_\mathrm{d}} u_\mathrm{d} \\ \frac{\mathrm{d}i_\mathrm{q}}{\mathrm{d}t} = -\frac{L_\mathrm{d}}{L_\mathrm{q}} \omega_\mathrm{e} i_\mathrm{d} - \frac{R_\mathrm{s}}{L_\mathrm{q}} i_\mathrm{q} + \frac{1}{L_\mathrm{q}} u_\mathrm{q} - \frac{\phi_\mathrm{f}}{L_\mathrm{q}} \omega_\mathrm{e} \end{cases} \tag{1}$$

where i_d and i_q are the direct and quadrature axis currents, respectively, measured in [A]; $R_\mathrm{s}, L_\mathrm{d}, L_\mathrm{q}$, and ϕ_f are phase resistance [Ω], d-axis inductance [H], q-axis inductance [H], and flux linkages [Wb] established by permanent magnets. The variable ω_e [rad/s] is the electrical rotor speed and equal to pole pairs p multiplied by the mechanical speed ω_m; $u_\mathrm{d}, u_\mathrm{q}$ are control inputs [V], used to control the behavior of the motor.

Considering the motor used in this article is surface-mounted type, it will have almost the same direct and quadrature axis magnetic reluctance, thus L_d and L_q are denoted as stator inductance L_s. The continuous state-space model of (1) is expressed as

$$\begin{cases} \dot{\boldsymbol{x}} = \mathbf{A}_\mathrm{c}\boldsymbol{x} + \mathbf{B}_\mathrm{c}\boldsymbol{u} + \mathbf{G}_\mathrm{vc} v \\ \boldsymbol{y} = \mathbf{C}_\mathrm{c}\boldsymbol{x} \end{cases} \tag{2}$$

where $\boldsymbol{x} = [i_\mathrm{d}, i_\mathrm{q}]^\mathrm{T}, \boldsymbol{u} = [u_\mathrm{d}, u_\mathrm{q}]^\mathrm{T}, v = \omega_\mathrm{e}$, and

$$\mathbf{A}_\mathrm{c} = \begin{bmatrix} -\frac{R_\mathrm{s}}{L_\mathrm{s}} & \omega_\mathrm{e} \\ -\omega_\mathrm{e} & -\frac{R_\mathrm{s}}{L_\mathrm{s}} \end{bmatrix}, \quad \mathbf{B}_\mathrm{c} = \begin{bmatrix} \frac{1}{L_\mathrm{s}} & 0 \\ 0 & \frac{1}{L_\mathrm{s}} \end{bmatrix}$$

$$\mathbf{G}_\mathrm{vc} = \begin{bmatrix} 0 \\ -\frac{\phi_\mathrm{f}}{L_\mathrm{s}} \end{bmatrix}, \mathbf{C}_\mathrm{c} = \begin{bmatrix} 1 & 0 \\ 0 & 1 \end{bmatrix}.$$

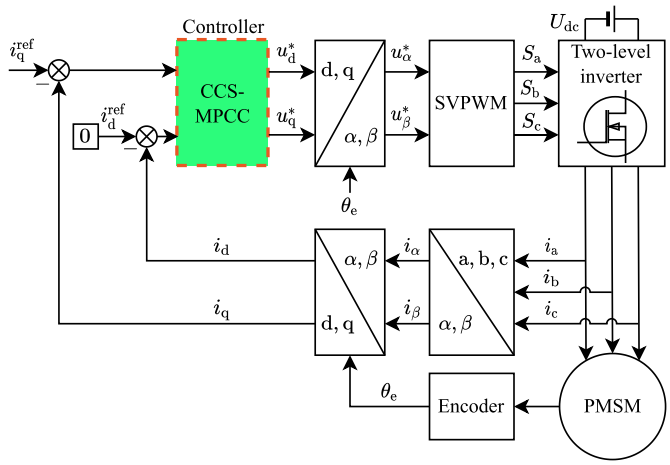

Fig. 1. Conventional FOC framework with CCS-MPCC.

In order to allow digital implementation, (2) needs to be discretized. The model expression discretized by the zero-order holder is shown as follows:

$$\begin{cases} \boldsymbol{x}(k+1) = \mathbf{A}\boldsymbol{x}(k) + \mathbf{B}\boldsymbol{u}(k) + \mathbf{G}_{\mathrm{v}} v(k) \\ \boldsymbol{y}(k) = \mathbf{C}\boldsymbol{x}(k) \end{cases} \tag{3}$$

where $\mathbf{A} = e^{\mathbf{A}_{\mathrm{c}} T_{\mathrm{s}}}$, $\mathbf{B} = \int_0^{T_{\mathrm{s}}} e^{\mathbf{A}_{\mathrm{c}} t} \mathrm{d}t \mathbf{B}_{\mathrm{c}}$, $\mathbf{C} = \mathbf{C}_{\mathrm{c}}$, $\mathbf{G}_{\mathrm{v}} = \int_0^{T_{\mathrm{s}}} e^{\mathbf{A}_{\mathrm{c}} t} \mathrm{d}t \mathbf{G}_{\mathrm{vc}}$, and T_{s} represents the sampling or control period.

III. Design of CCS-MPCC

The MPCC in this article is based on the FOC framework, which replaces the PI controller, as shown in Fig. 1. In order to maximize the torque output, the rotor current needs to lead the flux linkage by 90°. As a results, the goal of CCS-MPCC is to track quadrature axis current reference and keep direct current at zero.

A. Cost Function

The CCS-MPCC is realized by solving a cost function at each control period. In order to ensure the tracking performance and limit the output increment of the controller to avoid large overshoot, the cost function at time k can be described as follows [22]:

$$\min_{\Delta \boldsymbol{u}} \sum_{i=1}^{N_{\mathrm{p}}} \| \boldsymbol{y}_{i|k} - \boldsymbol{r}_{0|k} \|^2_{\mathbf{W}_{\boldsymbol{y}}} + \sum_{j=0}^{N_{\mathrm{u}}-1} \| \Delta \boldsymbol{u}_{j|k} \|^2_{\mathbf{W}_{\Delta \boldsymbol{u}}} \tag{4}$$

where $\boldsymbol{r}_{0|k} = [0, i_{\mathrm{q}}^{\mathrm{ref}}(k)]^{\mathrm{T}}$, $i_{\mathrm{q}}^{\mathrm{ref}}(k)$ is the reference of quadrature axis current, usually given by a speed loop controller. $\boldsymbol{y}_{i|k}$ is the system output predicted by model (3) based on state $\boldsymbol{x}(k)$, which means $\boldsymbol{y}_{i|k} = \mathbf{C}\boldsymbol{x}(k+i)$. N_{p} and N_{u} ($N_{\mathrm{p}} \geq N_{\mathrm{u}}$) are the prediction and control horizons, respectively. $\mathbf{W}_{\boldsymbol{y}}$ and $\mathbf{W}_{\Delta \boldsymbol{u}}$ are the weights of tracking performance and increment. $\Delta \boldsymbol{u}$ is the controller output incremental sequence, which is calculated by the following:

$$\Delta \boldsymbol{u} = \begin{bmatrix} \Delta \boldsymbol{u}_{0|k} \\ \Delta \boldsymbol{u}_{1|k} \\ \vdots \\ \Delta \boldsymbol{u}_{N_{\mathrm{u}}-1|k} \end{bmatrix}. \tag{5}$$

The elements of $\Delta \boldsymbol{u}$ is defined as

$$\Delta \boldsymbol{u}_{j|k} = \boldsymbol{u}_{j|k} - \boldsymbol{u}_{j-1|k}, j = 0, \ldots, N_{\mathrm{p}} - N_{\mathrm{u}} - 1$$
$$\boldsymbol{u}_{j|k} = \boldsymbol{u}(k+j).$$

By solving (4), the optimal control increment sequence at time k is obtained, but only the first control increment $\Delta \boldsymbol{u}_{0|k}$ is applied. As a results, the controller output is expressed by the following

$$\boldsymbol{u}(k) = \boldsymbol{u}(k-1) + \Delta \boldsymbol{u}_{0|k}. \tag{6}$$

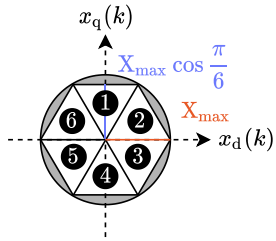

Fig. 2. Principle of polygonal approximation with six equal parts. $\mathrm{X}_{\max}$ is the maximum value of the circular constraint and the gray region is the neglected part.

B. Constraints

Subject to the power supply voltage and overcurrent capability of the motor, their constraints need to be considered in the process of solving (4). Consequently, the stator voltages and current in dq frame will be satisfied with the following:

$$\begin{cases} u_{\mathrm{d}}^2(k) + u_{\mathrm{q}}^2(k) & \leq \mathrm{U}_{\max} \\ i_{\mathrm{d}}^2(k) + i_{\mathrm{q}}^2(k) & \leq \mathrm{I}_{\max} \end{cases} \tag{7}$$

where $\mathrm{I}_{\max}$ is the maximum stator current allowed by the motor. $\mathrm{U}_{\max}$ is $\frac{1}{\sqrt{3}}$ of the bus voltage U_{dc}.

It is difficult to solve problem (4) that subject to (7) directly in real-time such as 10 kHz. However, a polygonal approximation method can be used to approximate (7) into a linear form. For example, Fig. 2 shows the schematic of six equal divisions briefly. $x_{\mathrm{d}}(k)$ and $x_{\mathrm{q}}(k)$ represent $u_{\mathrm{d}}(k)$ and $u_{\mathrm{q}}(k)$ or $i_{\mathrm{d}}(k)$ and $i_{\mathrm{q}}(k)$. $\mathrm{X}_{\max}$ is $\mathrm{U}_{\max}$ or $\mathrm{I}_{\max}$. The entire circular constraint is approximately divided into six linear regions. Assuming that the current or VV $\boldsymbol{x}_{\mathrm{s}} = [x_{\mathrm{d}}, x_{\mathrm{q}}]^{\mathrm{T}}$ is in region one, then the following approximate constraint needs to be satisfied:

$$\overbrace{\begin{bmatrix} 0 & 1 \end{bmatrix}}^{\boldsymbol{a}} \begin{bmatrix} x_{\mathrm{d}} \\ x_{\mathrm{q}} \end{bmatrix} \leq \mathrm{X}_{\max} \cos \frac{\pi}{6}. \tag{8}$$

In fact, the constraints of each linear region can be transformed into region 1 by rotation. For instance, when the vector is in

region 2, the constraints at this time will be the same as those described in (8) after rotating anticlockwise by $\frac{2\pi}{6}$ radians, which is

$$\boldsymbol{a}\overbrace{\begin{bmatrix}\cos\frac{2\pi}{6} & -\sin\frac{2\pi}{6}\\ \sin\frac{2\pi}{6} & \cos\frac{2\pi}{6}\end{bmatrix}}^{\mathbf{T}(6)}\begin{bmatrix}x_{\mathrm{d}}\\ x_{\mathrm{q}}\end{bmatrix}\le \mathrm{X}_{\max}\cos\frac{\pi}{6}. \tag{9}$$

Similarly, when the vector is in region q, the approximate constraint for the region is obtained by rotating it anticlockwise by $\frac{2\pi}{6}$ radians q times

$$\boldsymbol{a}\overbrace{\mathbf{T}(6)\ldots\mathbf{T}(6)}^{q\text{ times}}\begin{bmatrix}x_{\mathrm{d}}\\ x_{\mathrm{q}}\end{bmatrix}\le \mathrm{X}_{\max}\cos\frac{\pi}{6}. \tag{10}$$

When the constraints in all six regions are satisfied, the equivalent approximation constraint is expressed as follows:

$$\begin{bmatrix}\boldsymbol{a}\mathbf{T}^0(6)\\ \boldsymbol{a}\mathbf{T}^1(6)\\ \vdots\\ \boldsymbol{a}\mathbf{T}^5(6)\end{bmatrix}\boldsymbol{x}_{\mathrm{s}}(k)\le\begin{bmatrix}1\\1\\ \vdots\\1\end{bmatrix}\mathrm{X}_{\max}\cos\frac{\pi}{6}. \tag{11}$$

Therefore, constraint (7) will be divided equally by N_{cu} or N_{ci}, respectively, as shown as follows:

$$\begin{bmatrix}\boldsymbol{a}\mathbf{T}^0(N_{\mathrm{cu}})\\ \boldsymbol{a}\mathbf{T}^1(N_{\mathrm{cu}})\\ \vdots\\ \boldsymbol{a}\mathbf{T}^{N_{\mathrm{cu}}-1}(N_{\mathrm{cu}})\end{bmatrix}\boldsymbol{u}(k)\le\begin{bmatrix}1\\1\\ \vdots\\1\end{bmatrix}\mathrm{U}_{\max}\cos\frac{\pi}{N_{\mathrm{cu}}}$$

$$\begin{bmatrix}\boldsymbol{a}\mathbf{T}^0(N_{\mathrm{ci}})\\ \boldsymbol{a}\mathbf{T}^1(N_{\mathrm{ci}})\\ \vdots\\ \boldsymbol{a}\mathbf{T}^{N_{\mathrm{ci}}-1}(N_{\mathrm{ci}})\end{bmatrix}\boldsymbol{x}(k)\le\begin{bmatrix}1\\1\\ \vdots\\1\end{bmatrix}\mathrm{I}_{\max}\cos\frac{\pi}{N_{\mathrm{ci}}} \tag{12}$$

where $\mathbf{T}(n)$ is the rotation matrix, defined as follows:

$$\mathbf{T}(n)=\begin{bmatrix}\cos\frac{2\pi}{n} & -\sin\frac{2\pi}{n}\\ \sin\frac{2\pi}{n} & \cos\frac{2\pi}{n}\end{bmatrix}. \tag{13}$$

Cost function (4) and constraints (12) form an ideal model predictive controller.

IV. Design of Proposed MAESO-MPCC

While robustness is a important metric for controllers, high bandwidth is also a critical indicator for applications that require lower response time. In this article, an accurate MAESO is designed and compensated cycle-by-cycle to the predictive controller. In addition, a one-step delay is also considered to further improve the bandwidth performance.

A. CCS-MPCC in the Form of MPQP Problem

In order to achieve real-time computation, the cost function (4) needs to be converted into a MPQP problem. The matrix form of (4) at time $k+1$ is given by the following:

$$\min_{\boldsymbol{z}}\quad \mathbf{Y}^{\mathrm{T}}\mathbf{W}_{\mathrm{d}}\mathbf{Y}+\boldsymbol{z}^{\mathrm{T}}\mathbf{W}_{\delta\boldsymbol{u}}\boldsymbol{z} \tag{14}$$

$$\mathbf{W}_{\mathrm{d}}=\mathrm{Diagonal}(\mathbf{W}_{\boldsymbol{y}})_{N_{\mathrm{p}}\times N_{\mathrm{p}}},\ \mathbf{W}_{\delta\boldsymbol{u}}=\mathrm{Diagonal}(\mathbf{W}_{\Delta\boldsymbol{u}})_{N_{\mathrm{u}}\times N_{\mathrm{u}}}$$

$$\mathbf{Y}=\begin{bmatrix}\boldsymbol{y}_{1|k+1}-\boldsymbol{r}_{0|k+1}\\ \boldsymbol{y}_{2|k+1}-\boldsymbol{r}_{0|k+1}\\ \vdots\\ \boldsymbol{y}_{N_{\mathrm{p}}|k+1}-\boldsymbol{r}_{0|k+1}\end{bmatrix},\ \boldsymbol{z}=\begin{bmatrix}\Delta\boldsymbol{u}_{0|k+1}\\ \Delta\boldsymbol{u}_{1|k+1}\\ \vdots\\ \Delta\boldsymbol{u}_{N_{\mathrm{u}}-1|k+1}\end{bmatrix}.$$

Substituting the prediction (3) into (14) for predicting $\boldsymbol{y}_{i|k+1}, i=1,\ldots,N_{\mathrm{p}}$, the cost function is derived as follows:

$$\begin{aligned}\min_{\boldsymbol{z}}\quad & \boldsymbol{z}^{\mathrm{T}}(\mathbf{K}_1^{\mathrm{T}}\mathbf{W}_{\mathrm{d}}\mathbf{K}_1+\mathbf{W}_{\delta\boldsymbol{u}})\boldsymbol{z}+2\boldsymbol{x}_{0|k+1}^{\mathrm{T}}(\mathbf{PR})^{\mathrm{T}}\mathbf{W}_{\mathrm{d}}\mathbf{K}_1\boldsymbol{z}\\ &+2\boldsymbol{u}_{-1|k+1}^{\mathrm{T}}(\mathbf{PEM})^{\mathrm{T}}\mathbf{W}_{\mathrm{d}}\mathbf{K}_1\boldsymbol{z}+2v_{0|k+1}^{\mathrm{T}}(\mathbf{PSG}_{\mathrm{v}})^{\mathrm{T}}\mathbf{W}_{\mathrm{d}}\mathbf{K}_1\boldsymbol{z}\\ &-2\boldsymbol{r}_{0|k+1}^{\mathrm{T}}\mathbf{Q}^{\mathrm{T}}\mathbf{W}_{\mathrm{d}}\mathbf{K}_1\boldsymbol{z}+\text{constant}\end{aligned} \tag{15}$$

where $\boldsymbol{r}_{0|k+1}$ represent current reference of dq axis. $\boldsymbol{x}_{0|k+1}=\boldsymbol{x}(k+1)$ and $v_{0|k+1}=v(k+1)$ are feedback at time $k+1$. $\mathbf{K}_1=\mathbf{PEI}_m$. $\mathbf{P},\mathbf{E},\mathbf{I}_m,\mathbf{R},\mathbf{M},\mathbf{S}$, and $\mathbf{Q}$ are defined in (16) shown at the bottom of this page. $\mathbf{I}_2$ is the identity matrix with dimension 2.

Since the constant value does not affect the optimal solution, cost function (15) can be further simplified and rewritten as follows:

$$\min_{\boldsymbol{z}}\quad \frac{1}{2}\boldsymbol{z}^{\mathrm{T}}\mathbf{H}\boldsymbol{z}+\boldsymbol{\theta}_0^{\mathrm{T}}\mathbf{F}^{\mathrm{T}}\boldsymbol{z} \tag{17}$$

$$\mathbf{P}=\mathrm{Diagonal}(\mathbf{C})_{N_{\mathrm{p}}\times N_{\mathrm{p}}},\quad \mathbf{M}=\mathbf{Q}=[\mathbf{I}_2,\ldots,\mathbf{I}_2]^{\mathrm{T}}_{N_{\mathrm{p}}\times 1}$$

$$\mathbf{E}=\begin{bmatrix}\mathbf{B} & \mathbf{0} & \ldots & \mathbf{0}\\ \mathbf{AB} & \mathbf{B} & \ldots & \mathbf{0}\\ \vdots & \vdots & \ddots & \vdots\\ \mathbf{A}^{N_{\mathrm{p}}-1}\mathbf{B} & \mathbf{A}^{N_{\mathrm{p}}-2}\mathbf{B} & \ldots & \mathbf{B}\end{bmatrix}_{N_{\mathrm{p}}\times N_{\mathrm{p}}},\quad \mathbf{I}_m=\begin{bmatrix}\mathbf{I}_2 & \ldots & \mathbf{0}\\ \vdots & \ddots & \vdots\\ \mathbf{I}_2 & \ldots & \mathbf{I}_2\\ \mathbf{I}_2 & \ldots & \mathbf{I}_2\\ \vdots & \ddots & \vdots\\ \mathbf{I}_2 & \ldots & \mathbf{I}_2\end{bmatrix}_{N_{\mathrm{p}}\times N_{\mathrm{u}}},\quad \mathbf{R}=\begin{bmatrix}\mathbf{A}\\ \mathbf{A}^2\\ \vdots\\ \mathbf{A}^{N_{\mathrm{p}}}\end{bmatrix}_{N_{\mathrm{p}}\times 1},\quad \mathbf{S}=\begin{bmatrix}\mathbf{I}_2\\ \mathbf{A}+\mathbf{I}_2\\ \vdots\\ \sum_{i=0}^{N_{\mathrm{p}}-1}\mathbf{A}^i\end{bmatrix}_{N_{\mathrm{p}}\times 1} \tag{16}$$

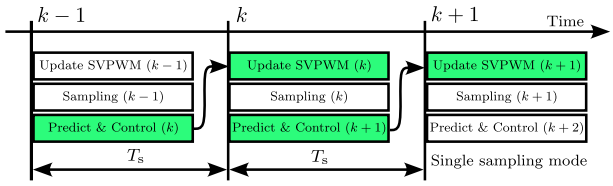

Fig. 3. One-step delay of digital system and single sampling mode.

where $\boldsymbol{\theta}_0$ is the feedback parameter of MPQP problem (17). $\mathbf{H}$, $\boldsymbol{\theta}_0$, and $\mathbf{F}$ are calculated by the following:

$$\begin{aligned}\mathbf{H} &= 2(\mathbf{K}_1^{\mathrm{T}}\mathbf{W}_{\mathrm{d}}\mathbf{K}_1 + \mathbf{W}_{\delta \boldsymbol{u}}) \\ \boldsymbol{\theta}_0 &= \begin{bmatrix} \boldsymbol{u}_{-1|k+1} \\ \boldsymbol{x}_{0|k+1} \\ \boldsymbol{r}_{0|k+1} \\ v_{0|k+1} \end{bmatrix}, \mathbf{F} = 2\begin{bmatrix} (\mathbf{PEM})^{\mathrm{T}}\mathbf{W}_{\mathrm{d}}\mathbf{K}_1 \\ (\mathbf{PR})^{\mathrm{T}}\mathbf{W}_{\mathrm{d}}\mathbf{K}_1 \\ -\mathbf{Q}^{\mathrm{T}}\mathbf{W}_{\mathrm{d}}\mathbf{K}_1 \\ (\mathbf{PSG}_{\mathrm{v}})^{\mathrm{T}}\mathbf{W}_{\mathrm{d}}\mathbf{K}_1 \end{bmatrix}^{\mathrm{T}}. \end{aligned} \tag{18}$$

B. CCS-MPCC With One-Step Delayed MAESO Compensation

Due to the variation of motor parameters, model (3) needs to be corrected in real-time for achieving more accurate prediction process

$$\begin{cases} \boldsymbol{x}(k+1) = \mathbf{A}\boldsymbol{x}(k) + \mathbf{B}\boldsymbol{u}(k) + \mathbf{G}_{\mathrm{v}}v(k) + \boldsymbol{f}(k) \\ \boldsymbol{y}(k) = \mathbf{C}\boldsymbol{x}(k) \end{cases} \tag{19}$$

where $\boldsymbol{f}(k) = [f_{\mathrm{d}}(k), f_{\mathrm{q}}(k)]^{\mathrm{T}}$ is model lumped disturbance that requires to be estimated to compensate for the prediction error when the motor parameters vary.

The model prediction error caused by parameter variation is obtained by the following MAESO:

$$\dot{\widetilde{\boldsymbol{x}}} = (\mathbf{A}_1 - \mathbf{L}\mathbf{C}_1)\widetilde{\boldsymbol{x}} + \mathbf{B}_1\boldsymbol{u} + \mathbf{G}_{\mathrm{vc1}}v + \mathbf{L}\boldsymbol{y} \tag{20}$$

where $\widetilde{\boldsymbol{x}} = \left[\hat{\boldsymbol{x}}^{\mathrm{T}}, \hat{\boldsymbol{f}}^{\mathrm{T}}\right]^{\mathrm{T}}$ is the estimation of state $\boldsymbol{x}$ and model lumped disturbance $\boldsymbol{f}$. $\mathbf{L}$ is the observer gain, and

$$\mathbf{A}_1 = \begin{bmatrix} \mathbf{A}_{\mathrm{c}} & \mathbf{I}_2 \\ \mathbf{0} & \mathbf{0} \end{bmatrix}, \mathbf{B}_1 = \begin{bmatrix} \mathbf{B}_{\mathrm{c}} \\ \mathbf{0} \end{bmatrix}$$

$$\mathbf{C}_1 = \begin{bmatrix} \mathbf{C}_{\mathrm{c}} & \mathbf{0} \end{bmatrix}, \mathbf{G}_{\mathrm{vc1}} = \begin{bmatrix} \mathbf{G}_{\mathrm{vc}} \\ \mathbf{0} \end{bmatrix}.$$

Using the first-order Euler method, the discretization of (20) can be expressed as follows:

$$\begin{aligned}\widetilde{\boldsymbol{x}}(k+1) &= \begin{bmatrix} \hat{\boldsymbol{x}}(k+1) \\ \hat{\boldsymbol{f}}(k+1) \end{bmatrix} \\ &= (T_{\mathrm{s}}(\mathbf{A}_1 - \mathbf{L}\mathbf{C}_1) + \mathbf{I})\widetilde{\boldsymbol{x}}(k) + T_{\mathrm{s}}\mathbf{B}_1\boldsymbol{u}(k) \\ &\quad + T_{\mathrm{s}}\mathbf{G}_{\mathrm{vc1}}v(k) + T_{\mathrm{s}}\mathbf{L}\boldsymbol{y}(k). \end{aligned} \tag{21}$$

In the digital system of the conventional FOC framework, the one-step delay problem shown in Fig. 3 must be considered and the controller output at time $k+1$ needs to be calculated at time k for the update of SVPWM module. Therefore, the state and disturbance at time k needs to be predicted for one step before

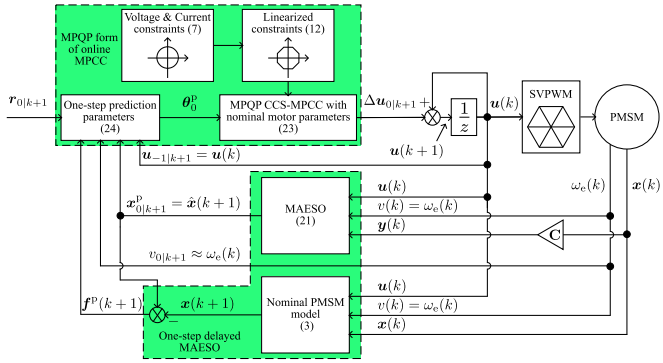

Fig. 4. Schematic of proposed MAESO-MPCC.

it can be used. As a result, the one step prediction of $\boldsymbol{x}(k)$ and $\boldsymbol{f}(k)$, $\boldsymbol{x}_{0|k+1}^{\mathrm{p}}$ and $\boldsymbol{f}^{\mathrm{p}}(k+1)$ are obtained by

$$\begin{cases} \boldsymbol{x}_{0|k+1}^{\mathrm{p}} = \hat{\boldsymbol{x}}(k+1) \\ \boldsymbol{f}^{\mathrm{p}}(k+1) = \hat{\boldsymbol{x}}(k+1) - \boldsymbol{x}(k+1). \end{cases} \tag{22}$$

In the prediction process, considering that the prediction horizon ($N_{\mathrm{p}}T_{\mathrm{s}}$) is much shorter than the mechanical time constant, it is reasonable that both the disturbance and speed remain unchanged. Therefore, $v_{0|k+1} = v(k+1) \approx \omega_{\mathrm{e}}(k)$ is assumed. Meanwhile, similar to (15), by substituting model (19) and (22) into (4), the CCS-MPCC with one-step delayed MAESO compensation is derived as follows:

$$\begin{aligned}\min_{\boldsymbol{z}} \quad & \frac{1}{2}\boldsymbol{z}^{\mathrm{T}}\mathbf{H}\boldsymbol{z} + (\boldsymbol{\theta}_0^{\mathrm{p}})^{\mathrm{T}}\left[\mathbf{F}, 2\mathbf{K}_1^{\mathrm{T}}\mathbf{W}_{\mathrm{d}}\mathbf{P}\mathbf{S}\right]^{\mathrm{T}}\boldsymbol{z} \\ \text{s.t.} \quad & \text{linear constraints (12)} \end{aligned} \tag{23}$$

where $\boldsymbol{\theta}_0^{\mathrm{p}}$ is one-step predictive parameter and described as follows:

$$\boldsymbol{\theta}_0^{\mathrm{p}} = \begin{bmatrix} \boldsymbol{u}_{-1|k+1} \\ \boldsymbol{x}_{0|k+1}^{\mathrm{p}} \\ \boldsymbol{r}_{0|k+1} \\ v_{0|k+1} \\ \boldsymbol{f}^{\mathrm{p}}(k+1) \end{bmatrix}. \tag{24}$$

The schematic of MAESO-MPCC is shown in Fig. 4. One-step delayed MAESO provides the estimated disturbances and the predicted feedback values as prediction parameters to MPCC for error compensation and online computation, thus a robust controller design is achieved.

C. Design of the MAESO Gain

The characteristic equation of the MAESO (20) is

$$|s\mathbf{I} - (\mathbf{A}_1 - \mathbf{L}\mathbf{C}_1)| = s^4 + as^3 + bs^2 + cs + d \tag{25}$$

where a, b, c, d are coefficients related to observer gain.

According to the desired bandwidth method and ensure the stability of the observer, the characteristic equation can also be expressed as follows:

$$|s\mathbf{I} - (\mathbf{A}_1 - \mathbf{L}\mathbf{C}_1)| = (s + \omega_{\mathrm{obs}})^4 \tag{26}$$

TABLE I
MOTOR PARAMETERS USED FOR VERIFICATION

Parameters	Symbols	Value	Unit
Phase resistance	R_s	0.5	Ω
Stator inductance	L_s	0.6555	mH
Magnet flux linkage	ϕ_f	6.6160	mWb
Pole pairs	p	8	–
Rated voltage	$\mathrm{U_{dc}}$	48	V
Rated torque	τ_r	0.27	Nm
Rated current	I_r	3.4	A

where ω_{obs} represents the observer bandwidth. The stability of the observer is guaranteed when ω_{obs} is greater than zero, which means that the poles of the observer all have negative real parts. Combine (25) and (26), the observer gain is computed as follows:

$$\mathbf{L}=\begin{bmatrix} 2\omega_{\mathrm{obs}}+v-\frac{R_\mathrm{s}}{L_\mathrm{s}} & 0 \\ 0 & 2\omega_{\mathrm{obs}}-v-\frac{R_\mathrm{s}}{L_\mathrm{s}} \\ \omega_{\mathrm{obs}}^2 & 0 \\ 0 & \omega_{\mathrm{obs}}^2 \end{bmatrix}. \tag{27}$$

The gain of conventional ESO retains the terms related to ω_{obs} only. However, this simplification does not take model information into account well. Therefore, in order to make the observer closer to the real system and to estimate the disturbances more efficiently, the measurable disturbance v is retained in this article. Thus, $\mathbf{L}$ is simplified to

$$\mathbf{L}\approx\begin{bmatrix} 2\omega_{\mathrm{obs}}+v & 0 \\ 0 & 2\omega_{\mathrm{obs}}-v \\ \omega_{\mathrm{obs}}^2 & 0 \\ 0 & \omega_{\mathrm{obs}}^2 \end{bmatrix}. \tag{28}$$

V. SIMULATION AND EXPERIMENTAL VERIFICATION

To verify the effectiveness of the proposed method, simulations and experiments are carried out. The motor parameters used for verification are listed in Table I.

Verification consists of two parts. On one hand, the proposed MAESO-MPCC method is implemented. By using different motor parameters for the same motor, the compensation results and control performance of this method are verified. On the other hand, the PI controller and integral action-based MPCC (IA-MPCC) [22] are implemented for the current loop and used for comparison with the MAESO-MPCC method to illustrate the effect of the latter. In order to evaluate the performance of the loop controller, a conventional PI controller is implemented for the speed loop, which is used to invoke the current loop. Except for the motor parameters, all other control parameters during the verification process remain unchanged.

After proper simplification, the current loop parameters K_p and K_i based on the PI controller are calculated [33] by (29) in this article.

$$\begin{cases} K_\mathrm{p}=L_\mathrm{s}\omega_{\mathrm{db}} \\ K_\mathrm{i}=R_\mathrm{s}/L_\mathrm{s} \end{cases} \tag{29}$$

TABLE II
PARAMETERS OF THE HARDWARE

Parameters	T_s	Sampling method
Value	100 µs	Single sampling

TABLE III
PARAMETERS OF THE MAESO-MPCC

Symbols	N_p	N_u	N_cu	N_ci	$\mathbf{W}_{\boldsymbol{y}}$	$\mathbf{W}_{\Delta\boldsymbol{u}}$	$\mathrm{I_{max}}$	$\mathrm{U_{max}}$
Value	2	1	6	8	$\mathbf{I}_2$	$0.1\mathbf{I}_2$	5 A	$\frac{48}{\sqrt{3}}$ V

TABLE IV
DIFFERENT MOTOR PARAMETER CONDITIONS

Condition	Motor parameters
C1	R_s, L_s and ϕ_f
C2	$10\%R_\mathrm{s}$, $50\%L_\mathrm{s}$ and $200\%\phi_\mathrm{f}$
C3	$500\%R_\mathrm{s}$, $200\%L_\mathrm{s}$ and $50\%\phi_\mathrm{f}$

where ω_{db} is the desired bandwidth.

A. Parameter Settings

The hardware parameters including sampling period T_s and method are listed in Table II. Both the sampling and control period used in the experiments are T_s. In addition, the parameters of MAESO-MPCC are listed in Table III.

Increasing N_p and N_u will lead to inaccurate prediction steps and a more conservative controller. Therefore, N_p and N_u are set to 2 and 1. The larger the N_{cu} and N_{ci}, the higher the number of constraints will be, which makes the computational effort increase significantly. This is a trade-off between computational effort and model simplification. To achieve a reasonable approximation, $N_{\mathrm{cu}}=6$ and $N_{\mathrm{ci}}=8$ are set in this article, respectively. The choice between $\mathbf{W}_{\boldsymbol{y}}$ and $\mathbf{W}_{\Delta\boldsymbol{u}}$ depends on the ratio of them. Increasing the ratio of $\mathbf{W}_{\boldsymbol{y}}$ means improving the tracking performance during prediction, and $\mathbf{W}_{\Delta\boldsymbol{u}}$ represents a slow controller increment. Therefore, $\mathbf{W}_{\boldsymbol{y}}$ is chosen to be ten times of $\mathbf{W}_{\Delta\boldsymbol{u}}$ in this article to ensure the tracking performance of the controller.

B. Simulation Results

The simulation works in speed closed loop mode and the speed reversal experiment is implemented. At the time of 0.05 s, the speed reference is changed from -1000 r/min to 1000 r/min. During this transient, the current loop will produce an ideal step response under the action of the speed loop. In order to verify the robustness of the proposed method, different motor mismatch parameter conditions will be applied to the controller and these conditions are summarized in Table IV. Further, the root mean square (RMS) of the current tracking error e can be used to evaluate the tracking performance of different current

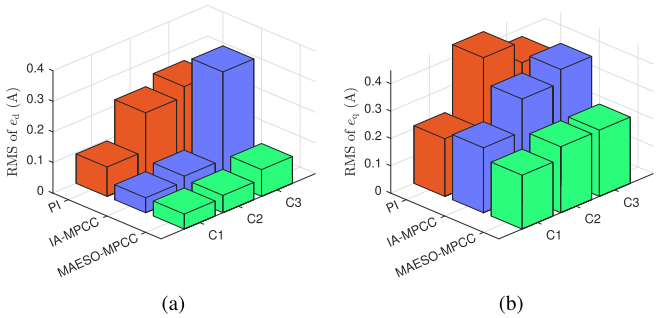

Fig. 5. Simulation results of current tracking error RMS using different controller under different motor parameters. (a) d-axis. (b) q-axis.

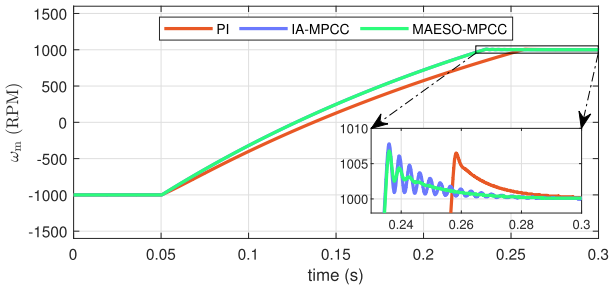

Fig. 6. Speed reversal response using different controllers with C2 condition.

controllers, which is calculated as follows.

$$\mathrm{RMS}(e) = \sqrt{\frac{1}{\mathrm{length}(e)} \sum_{i=1}^{\mathrm{length}(e)} e^2(i)} \tag{30}$$

Fig. 5 shows the simulation results of current tracking performance of different controllers including PI, IA-MPCC, and the proposed method with different motor parameter conditions C1, C2, and C3 summarized in Table IV. Taking Fig. 5(a) as an example, for the same controller, the *d*-axis current tracking error RMS increases with the mismatch of motor parameters, such as C2 and C3, which is reasonable. However, MAESO-MPCC has only 0.09 A current tracking error RMS value with C3 condition compared to 0.25 A for PI and 0.35 A for IA-MPCC, which indicates that the proposed method has well immunity to parameter mismatch. Meanwhile, similar conclusions can be obtained for C2 in Fig. 5(a) and C1 to C3 in Fig. 5(b).

Fig. 6 shows the simulation results of the speed loop response using different controllers under C2 conditions. It is clear that the speed loop settling time using PI controller is longer compared to IA-MPCC and MAESO-MPCC. Also, although the response times are almost the same, the proposed method is smoother during the transients compared to IA-MPCC.

C. Experimental Results

In order to verify the effectiveness of the proposed method comprehensively, the conventional ESO-MPCC method and the method mentioned in the simulation are implemented for experimental comparison during load disturbance, speed reversal,

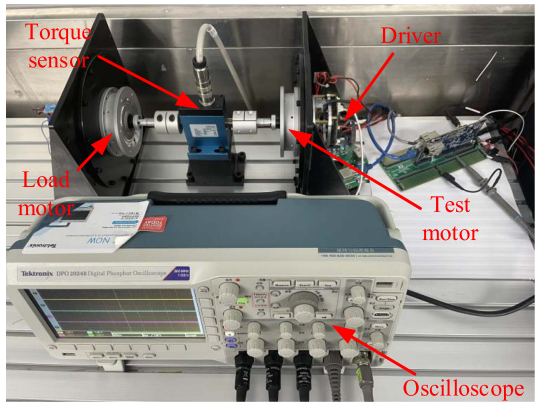

Fig. 7. Test bench with PMSM driver, torque sensor, oscilloscope, load, and test motor.

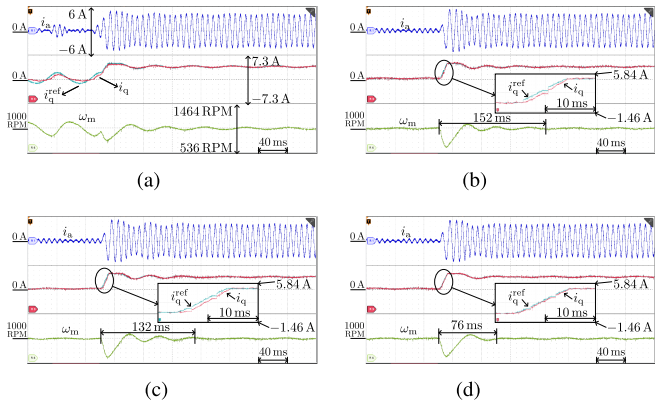

Fig. 8. Experimental results of load disturbance under different methods with C2 condition. The offset of ω_m is 1000 r/min. (a) PI. (b) ESO-MPCC. (c) IA-MPCC. (d) MAESO-MPCC.

current loop frequency response characteristics, and inverter dead-time disturbance experiments.

The inverter includes a digital signal processor (DSP) TMS320F28375D produced by Texas Instruments. It is a dual-core CPU with floating point arithmetic unit. CPU1 is used for the digital implementation of the controller, and CPU2 is used for communication processing. The test bench is shown in Fig. 7.

Except for the current controller, other control parameters are kept the same. The desired bandwidth ω_{db} of the PI controller is set as an engineering empirical value, which is one-twentieth of the control frequency. The observer gains in both ESO-MPCC and IA-MPCC are well adjusted to ensure stability, while other parameters are consistent with the proposed method.

1) Performance of Load Disturbance Experiment: The test motor is operated in current mode under C2 condition while the load motor is kept in 1000 r/min using speed mode. At the time of 0.1 s, 100 % of the rated torque is applied to the test motor. The current loop performance difference of tracking error between the different methods for this disturbance can be shown in Figs. 8 and 9(a).

Fig. 8 shows that under the model mismatch condition C2, the PI controller is unstable. MAESO-MPCC has the smallest speed

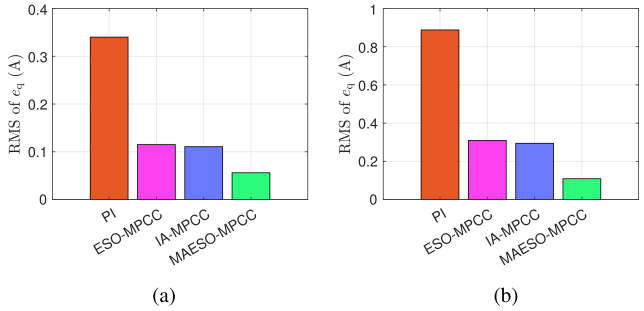

Fig. 9. RMS value of q-axis current tracking error using different controllers under C2 condition. (a) Load disturbance. (b) Speed reversal.

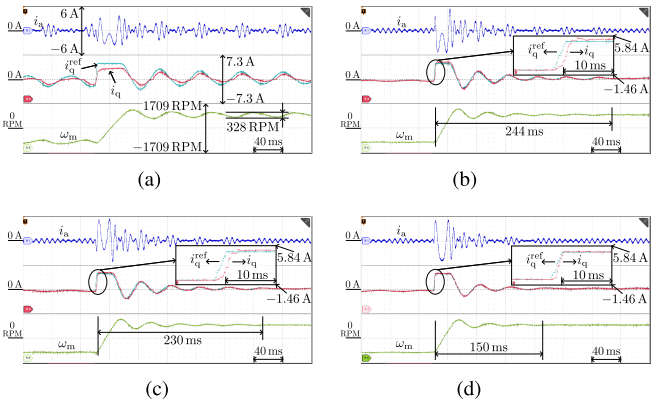

Fig. 10. Experimental results of speed reversal under different methods with C2 condition. (a) PI. (b) ESO-MPCC. (c) IA-MPCC. (d) MAESO-MPCC.

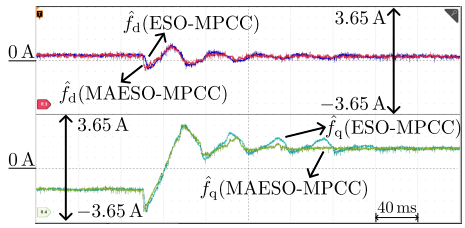

Fig. 11. Estimated lumped disturbance of speed reversal with C2 condition.

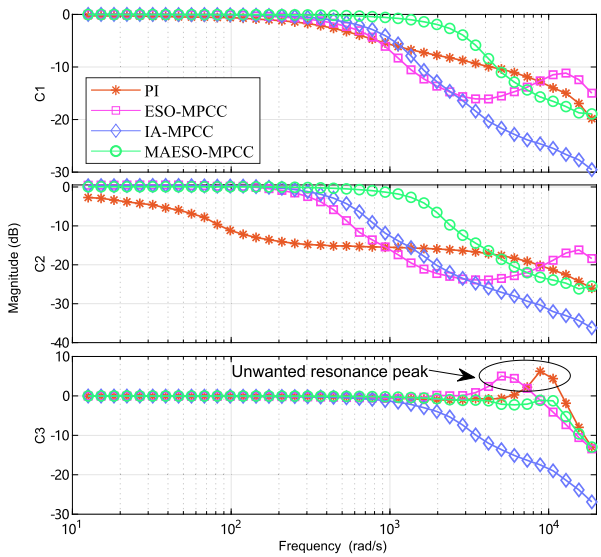

Fig. 12. Frequency response of the current loop with different controllers and with different motor parameters.

settling time of 76 ms and well current tracking performance in the partially enlarged subfigure. Moreover, as can be seen in Fig. 9(a), proposed method has a current tracking error RMS value of only 0.06 A for sudden load changes, while the PI, ESO-MPCC, and IA-MPCC are 0.34 A, 0.12 A, and 0.11 A, respectively, which are significantly larger than the proposed method.

2) Performance of Speed Reversal Experiment: In order to remove the load disturbance and to operate in the speed mode under C2 condition, the load was disconnected from the motor in this experiment. Then, at the time of 0.1 s, the reference speed was suddenly changed from −1000 r/min to 1000 r/min. It is clear from Fig. 10(a) that the PI controller does not satisfactory feed the current during speed reversal and a large ripple of 328 r/min can be observed. Proposed MAESO-MPCC in Fig. 10(d), instead, is stable and has a speed settling time of only 150 ms. Other MPCC-based methods, even making the speed loop stable, require longer settling times with 244 ms and 230 ms in Fig. 10(b) and (c). Meanwhile, the partially enlarged subfigure indicates that the proposed method is much faster than other methods in current tracking. In Fig. 9(b), the proposed method has the smallest current tracking error RMS value of 0.11 A, which is significantly lower than other methods with 0.89 A, 0.31 A, and 0.29 A. It is worth noting that the current highest tracking error drops from 3.34 A in Fig. 10(c) to 1.69 A in Fig. 10(d), indicating that the proposed method still maintains sufficient bandwidth performance.

Since only the ESO-MPCC and MAESO-MPCC methods estimated the disturbances, Fig. 11 presents the estimated $\hat{f}_d$ and $\hat{f}_q$ for the dq-axis during speed reversal. In fact, the reference curve of d-axis lumped disturbance should be a straight line while the q-axis should be a ramp related to the speed. It can be observed that the proposed method for the estimation of the lumped disturbances, especially for the q-axis, has a faster convergence rate compared to the conventional ESO-MPCC and thus provide a sufficiently better compensation result.

3) Performance of Frequency Response Experiment: In this experiment, the motor is operated in current loop mode with no load. A sinusoidal current signal from 2 to 2975 Hz with an amplitude of 0.7 A is applied to the current loop under C1, C2, or C3 condition to obtain its frequency response. The bandwidth of the system is defined as the frequency corresponding to the drop in response value to −3 dB. The results of experiments are summarized in Fig. 12 and Table V.

From the results, different parameter conditions may lead to an increased or decreased bandwidth. When the controller use nominal motor parameters, i.e., C1 condition, all controllers have the expected bandwidth performance. Under C2 condition, the bandwidth of the PI controller shows a significant decrease from 533 to 44 rad/s, which is about ten times lower. In fact, when specifying the reference system bandwidth ω_{db}^{ref}, the bandwidth of PI controller ω_{db}^{C1} and ω_{db}^{C2} under C1 and C2 condition

TABLE V
PERFORMANCE INDICATORS OF DIFFERENT METHODS

Control technique		PI	ESO-MPCC	IA-MPCC	MAESO-MPCC
Computation time (μs)		2.13	43.85	43.38	**44.01**
Load disturbance experiment	Maximum tracking error of i_q (A)	1.03	0.74	0.73	**0.34**
	Settling time of speed (ms)	-	152	132	**76**
	Steady state error of speed (RPM)	-	-0.81	-0.61	**0.44**
Speed reversal experiment	Maximum tracking error of i_q (A)	3.33	3.30	3.34	**1.69**
	Overshooting of speed (%)	**16.98**	20.53	20.80	18.48
	Settling time of speed (ms)	-	244	230	**150**
	Steady state error of speed (RPM)	-	-0.54	0.48	**0.16**
Current closed loop bandwidth	Nominal model (rad/s)	533	628	791	**2509**
	Mismatch model with C2 (rad/s)	44	308	426	**1410**
	Mismatch model with C3 (rad/s)	**13333**	9982	1651	11578

can be derived theoretically from (29) as follows:

$$\begin{cases} K_{\mathrm{p}}^{\mathrm{C1}} K_{\mathrm{i}}^{\mathrm{C1}} = L_{\mathrm{s}} \omega_{\mathrm{db}}^{\mathrm{ref}} \cdot \frac{R_{\mathrm{s}}}{L_{\mathrm{s}}} = R_{\mathrm{s}} \omega_{\mathrm{db}}^{\mathrm{C1}} \\ K_{\mathrm{p}}^{\mathrm{C2}} K_{\mathrm{i}}^{\mathrm{C2}} = 50\% L_{\mathrm{s}} \omega_{\mathrm{db}}^{\mathrm{ref}} \cdot \frac{10\% R_{\mathrm{s}}}{50\% L_{\mathrm{s}}} = R_{\mathrm{s}} \omega_{\mathrm{db}}^{\mathrm{C2}} \end{cases} \Rightarrow \omega_{\mathrm{db}}^{\mathrm{C2}} = \frac{1}{10} \omega_{\mathrm{db}}^{\mathrm{C1}}. \tag{31}$$

ESO-MPCC and IA-MPCC, on the other hand, have fundamental parametric robustness, so their bandwidths are only reduced from 628 to $308\,\mathrm{rad/s}$ and 791 to $426\,\mathrm{rad/s}$, respectively. The bandwidth of MAESO-MPCC remains at $1410\,\mathrm{rad/s}$ due to the accurate and timely estimation by the observer, indicating that the proposed method has a better robust performance for the motor parameters. With the condition C3, a noticeable increase in bandwidth can be observed. Due to the unmodeled dynamics such as pole, both PI and ESO-MPCC present unwanted resonance peak, proposed method, instead, suppresses such a phenomenon because it compensates for the model uncertainty in real-time. IA-MPCC does not have any resonance peak because the method itself introduces an integrator that brings a zero to the system, causing a zero-pole cancellation with the unmodeled pole. However, this also makes it difficult to further extend the bandwidth.

4) Performance of Inverter Dead-Time Disturbance Experiment: In order to verify the performance of the controller to compensate for inverter dead-time, the bandwidth test experiment with different dead-time under nominal motor parameters, i.e. C1 condition, are carried out. By setting several inverter dead-time (1 and $2\,\mu\mathrm{s}$), the bandwidth results for different controllers are presented in Fig. 13. As the dead-time increases, the nonlinearity of the system also increases. Therefore, it is reasonable that the bandwidth performance of the controller will all decrease. In particular, the PI controller, whose bandwidth is reduced from 2076 to $788\,\mathrm{rad/s}$ when the inverter dead-time is increased from 1 to $1.5\,\mu\mathrm{s}$, indicates that the dead-time has a significant impact on its bandwidth. However, it is notable that MAESO-MPCC has a satisfactory bandwidth performance regardless of the dead-time variation. Even when the dead-time is $2\,\mu\mathrm{s}$, the bandwidth of the proposed method is $2509\,\mathrm{rad/s}$, which is still higher than the bandwidth of other controllers when the dead-time is $1\,\mu\mathrm{s}$.

5) Summary of Experiments: The performance indicators, including the controller computation time, are summarized in Table V. Compared with the PI controller, the time consumed by the proposed method is increased by $41.88\,\mu\mathrm{s}$, but this will bring a significant improvement in the tracking performance, especially when there is a mismatch in the model. In addition, it is only 0.63 and $0.16\,\mu\mathrm{s}$ higher than the existing IA-MPCC method and ESO-MPCC method, which does not require additional computing resources for the processor. The experimental results show that the proposed method has significant robustness improvement in the presence of nonlinear factors such as large dead-time or model mismatch. Since the proposed method is able to compensate the prediction error in time cycle by cycle, the system bandwidth is theoretically enhanced. Although the experiments are carried out with low power motors, the proposed method is general and can be easily extended to drive systems of any power level to enhance the dynamic performance of their applications.

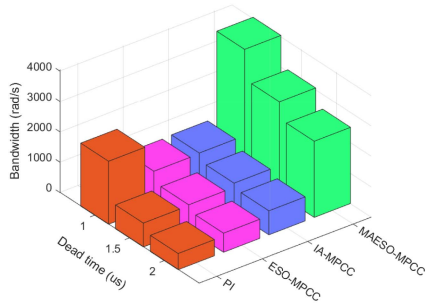

Fig. 13. Bandwidth results of respective controller with different inverter dead-time under nominal model.

VI. CONCLUSION

A novel real-time MPCC method for PMSM drives based on MAESO compensation was proposed in this article. It offers higher bandwidth and enhanced parameter robustness performance over existing MPCC. The conventional MPCC was modified into the form of MPQP and the nonlinear constraints of the controller are approximated as linear constraints by the polygonal linear method, which reduced the complexity of the real-time solution of the controller. Further, to improve the robustness of the controller to model mismatches, the MAESO

was designed to estimate these predictive errors quickly and accurately at each control cycle. Simulation and experimental results demonstrate that proposed method improves the dynamic response of the current loop under different operating conditions with model mismatch. Besides, experiments on the controller bandwidth under different motor parameters and different inverter dead-time show that proposed method has the ability to provide high bandwidth performance for some applications requiring lower response time, which effectively demonstrates the practical value of the proposed method.

REFERENCES

[1] M. Wang, D. Sun, W. Ke, and H. Nian, "A universal lookup table-based direct torque control for OW-PMSM drives," *IEEE Trans. Power Electron.*, vol. 36, no. 6, pp. 6188–6191, Jun. 2021.

[2] Z. Liu, W. Lin, X. Yu, J. J. Rodríguez-Andina, and H. Gao, "Approximation-free robust synchronization control for dual-linear-motors-driven systems with uncertainties and disturbances," *IEEE Trans. Ind. Electron.*, vol. 69, no. 10, pp. 10 500–10 509, Oct. 2022.

[3] Z. Li, F. Wang, D. Ke, J. Li, and W. Zhang, "Robust continuous model predictive speed and current control for PMSM with adaptive integral sliding-mode approach," *IEEE Trans. Power Electron.*, vol. 36, no. 12, pp. 14 398–14 408, Dec. 2021.

[4] S. Vazquez, J. Rodriguez, M. Rivera, L. G. Franquelo, and M. Norambuena, "Model predictive control for power converters and drives: Advances and trends," *IEEE Trans. Ind. Electron.*, vol. 64, no. 2, pp. 935–947, Feb. 2017.

[5] W. Lu et al., "Load adaptive PMSM drive system based on an improved ADRC for manipulator joint," *IEEE Access*, vol. 9, pp. 33 369–33 384, 2021.

[6] S. Fang, Y. Wang, W. Wang, Y. Chen, and Y. Chen, "Design of permanent magnet synchronous motor servo system based on improved particle swarm optimization," *IEEE Trans. Power Electron.*, vol. 37, no. 5, pp. 5833–5846, May 2022.

[7] K.-M. Choo and C.-Y. Won, "Design and analysis of electrical braking torque limit trajectory for regenerative braking in electric vehicles with PMSM drive systems," *IEEE Trans. Power Electron.*, vol. 35, no. 12, pp. 13 308–13 321, Dec. 2020.

[8] S. Hu, Z. Liang, W. Zhang, and X. He, "Research on the integration of hybrid energy storage system and dual three-phase PMSM drive in EV," *IEEE Trans. Ind. Electron.*, vol. 65, no. 8, pp. 6602–6611, Aug. 2018.

[9] D. Novotny and T. Lipo, *Vector Control and Dynamics of AC Drives*. Oxford, U.K.: Claredon Press, 1998.

[10] J. Rodriguez et al., "Latest advances of model predictive control in electrical drives-part I: Basic concepts and advanced strategies," *IEEE Trans. Power Electron.*, vol. 37, no. 4, pp. 3927–3942, Apr. 2022.

[11] J. Rodriguez et al., "Latest advances of model predictive control in electrical drives-part II: Applications and benchmarking with classical control methods," *IEEE Trans. Power Electron.*, vol. 37, no. 5, pp. 5047–5061, May 2022.

[12] X. Li, W. Tian, X. Gao, Q. Yang, and R. Kennel, "A generalized observer-based robust predictive current control strategy for PMSM drive system," *IEEE Trans. Ind. Electron.*, vol. 69, no. 2, pp. 1322–1332, Feb. 2022.

[13] Z. Zhang, Z. Wang, X. Wei, Z. Liang, R. Kennel, and J. Rodriguez, "Space-vector-optimized predictive control for dual three-phase PMSM with quick current response," *IEEE Trans. Power Electron.*, vol. 37, no. 4, pp. 4453–4462, Apr. 2022.

[14] Y. Liu, J. Gao, B. Zhan, and L. Zhang, "Impact force control of high-speed wire bonding machine based on fuzzy active disturbance rejection controller," in *Proc. 22nd Int. Conf. Electron. Packag. Technol.*, 2021, pp. 1–6.

[15] G. Hu, J. Ma, Y. Zuo, Y. Wang, H. Yan, and Q. Lv, "A flexible velocity planning algorithm for high-speed mounter with both efficiency and precision," *J. Braz. Soc. Mech. Sci. Eng.*, vol. 43, no. 12, pp. 1–18, 2021, doi: 10.1007/s40430-021-03233-9.

[16] F. Wang, L. He, and J. Rodriguez, "FPGA-based continuous control set model predictive current control for PMSM system using multistep error tracking technique," *IEEE Trans. Power Electron.*, vol. 35, no. 12, pp. 13 455–13 464, Dec. 2020.

[17] A. Brosch, O. Wallscheid, and J. Böcker, "Model predictive control of permanent magnet synchronous motors in the overmodulation region including six-step operation," *IEEE Open J. Ind. Appl.*, vol. 2, no. 1, pp. 47–63, Mar. 2021, doi: 10.1109/OJIA.2021.3066105.

[18] B. Wang, Z. Dong, Y. Yu, G. Wang, and D. Xu, "Static-errorless deadbeat predictive current control using second-order sliding-mode disturbance observer for induction machine drives," *IEEE Trans. Power Electron.*, vol. 33, no. 3, pp. 2395–2403, Mar. 2018.

[19] C. Wang, M. Yang, W. Zheng, J. Long, and D. Xu, "Vibration suppression with shaft torque limitation using explicit MPC-PI switching control in elastic drive systems," *IEEE Trans. Ind. Electron.*, vol. 62, no. 11, pp. 6855–6867, Nov. 2015.

[20] M. R. Nikzad, B. Asaei, and S. O. Ahmadi, "Discrete duty-cycle-control method for direct torque control of induction motor drives with model predictive solution," *IEEE Trans. Power Electron.*, vol. 33, no. 3, pp. 2317–2329, Mar. 2018.

[21] M. Aguirre, S. Kouro, C. A. Rojas, and S. Vazquez, "Enhanced switching frequency control in FCS-MPC for power converters," *IEEE Trans. Ind. Electron.*, vol. 68, no. 3, pp. 2470–2479, Mar. 2021.

[22] G. Cimini, D. Bernardini, S. Levijoki, and A. Bemporad, "Embedded model predictive control with certified real-time optimization for synchronous motors," *IEEE Trans. Control Syst. Technol.*, vol. 29, no. 2, pp. 893–900, Mar. 2021.

[23] J. Long, M. Yang, Y. Chen, K. Liu, and D. Xu, "Current-controller-free self-commissioning scheme for deadbeat predictive control in parametric uncertain SPMSM," *IEEE Access*, vol. 9, pp. 289–302, 2021.

[24] C. Xiong, H. Xu, T. Guan, and P. Zhou, "A constant switching frequency multiple-vector-based model predictive current control of five-phase pmsm with nonsinusoidal back EMF," *IEEE Trans. Ind. Electron.*, vol. 67, no. 3, pp. 1695–1707, Mar. 2020.

[25] X. Zhang, L. Zhang, and Y. Zhang, "Model predictive current control for PMSM drives with parameter robustness improvement," *IEEE Trans. Power Electron.*, vol. 34, no. 2, pp. 1645–1657, Feb. 2019.

[26] C. Ma, H. Li, X. Yao, Z. Zhang, and F. De Belie, "An improved model-free predictive current control with advanced current gradient updating mechanism," *IEEE Trans. Ind. Electron.*, vol. 68, no. 12, pp. 11968–11979, Dec. 2021.

[27] F. Tinazzi, P. G. Carlet, S. Bolognani, and M. Zigliotto, "Motor parameter-free predictive current control of synchronous motors by recursive least-square self-commissioning model," *IEEE Trans. Ind. Electron.*, vol. 67, no. 11, pp. 9093–9100, Nov. 2020.

[28] Y. Zhang, J. Jin, and L. Huang, "Model-free predictive current control of PMSM drives based on extended state observer using ultralocal model," *IEEE Trans. Ind. Electron.*, vol. 68, no. 2, pp. 993–1003, Feb. 2021.

[29] M. Yang, X. Lang, J. Long, and D. Xu, "Flux immunity robust predictive current control with incremental model and extended state observer for PMSM drive," *IEEE Trans. Power Electron.*, vol. 32, no. 12, pp. 9267–9279, Dec. 2017.

[30] Y. Xu, B. Zheng, G. Wang, H. Yan, and J. Zou, "Current harmonic suppression in dual three-phase permanent magnet synchronous machine with extended state observer," *IEEE Trans. Power Electron.*, vol. 35, no. 11, pp. 12 166–12 180, Nov. 2020.

[31] W. Xu, A. K. Junejo, Y. Liu, M. G. Hussien, and J. Zhu, "An efficient antidisturbance sliding-mode speed control method for PMSM drive systems," *IEEE Trans. Power Electron.*, vol. 36, no. 6, pp. 6879–6891, Jun. 2021.

[32] H. Liu and S. Li, "Speed control for PMSM servo system using predictive functional control and extended state observer," *IEEE Trans. Ind. Electron.*, vol. 59, no. 2, pp. 1171–1183, Feb. 2012.

[33] X. Fu, H. He, Y. Xu, and X. Fu, "A strongly robust and easy-tuned current controller for PMSM considering parameters variation," *IEEE Access*, vol. 8, pp. 44 228–44 238, 2020.

Huanli Liu was born in Hunan, China, in 1996. He received the B.S. degree in electrical engineering from Shenyang University of Technology, Shenyang, China, in 2018. He is currently working toward the Ph.D. degree in control science and engineer with Harbin Institute of Technology, Harbin, China. His research interests include permanent-magnet machine drives and predictive control.

Weiyang Lin (Member, IEEE) received the B.S., M.Sc., and Ph.D. degrees in mechanical engineering from the Harbin Institute of Technology, Harbin, China, in 2006, 2008, and 2014, respectively. He is currently an Associate Professor with the Research Institute of Intelligent Control and Systems, Harbin Institute of Technology. His research interests include parallel manipulators, robotic motion control, and visual servoing.

Zhitai Liu (Student Member, IEEE) was born in Shandong, China, in 1995. He received the B.S. degree in automation from Qingdao University, Qingdao, China, in 2017, and the M.S. degree in control science and engineer in 2019 from Harbin Institute of Technology, Harbin, China, where he is currently working toward the Ph.D. degree in control science and engineer. His research interests include motion control, mechatronics, and embedded systems.

Concettina Buccella (Senior Member, IEEE) received the M.Sc. degree from the University of L'Aquila, L'Aquila, Italy, in 1988, and the Ph.D. degree in electrical engineering from the University of Rome "La Sapienza," Rome, in 1995.

From 1988 to 1989, she was a R&D Engineer with Italtel SpA, L'Aquila, Italy. In 1991, joined the University of L'Aquila, where she is a Professor of Power Converters, Electric Machines, and Drives and the Chair of the B.Sc. in ICT Engineering. Her current research interests include modulation techniques for power converters, renewable energy, smart grids, analytical and numerical modeling of electric systems. Prof. Buccella was a corecipient of the 2012 and the 2013 Best Paper Award of the IEEE TRANSACTIONS ON INDUSTRIAL INFORMATICS. She has been an Associate Editor for the IEEE TRANSACTIONS ON INDUSTRIAL ELECTRONICS, and for the IEEE SYSTEMS JOURNAL. From 2017 to 2018, she was the Chair of the IEEE-IES Technical Committee on Renewable Energy Systems. She is the Chief Scientific Officer with DigiPower Ltd., L'Aquila, Italy, a R&D company active in the field of power electronics.

Carlo Cecati (Fellow, IEEE) received the Dr. Ing. degree in electrotechnical engineering from the University of L'Aquila, L'Aquila, Italy,, in 1983.

Since then, he has been with the same university where he is a Professor of Industrial Electronics and Drives since 2006. From 2015 to 2017, he has been a Qianren Talents Professor with the Harbin Institute of Technology, Harbin, China. His primarily research interests include power electronics, distributed generation, e-transportation and smart grids.

Prof. Cecati has been Co-Editor-in-Chief (2010–2012) and Editor-in-Chief (2013–2015) of the IEEE TRANSACTIONS ON INDUSTRIAL ELECTRONICS. He has been a corecipient of the 2012 and the 2013 Best Paper Award from the IEEE TRANSACTIONS ON INDUSTRIAL INFORMATICS, of the 2012 Best Paper Award from the IEEE INDUSTRIAL ELECTRONICS MAGAZINE and of the 2019 Outstanding Paper Award from the IEEE Transactions on Industrial Electronics. In 2017, he received the Antony J. Hornfeck Award from the IEEE Industrial Electronics Society, in 2019 received the title of "Commander of the Republic of Italy" from the President of the Republic of Italy, in 2021 he received the Eugene Mittlemann Achievement Award from the IEEE. He is Chief Technical Officer at DigiPower Ltd., a R&D company active in the field of power electronics.